

IN-FLIGHT SURFACE-FLOW MEASUREMENTS ON A SUBSONIC TRANSPORT HIGH-LIFT FLAP SYSTEM

Long P. Yip
 NASA Langley Research Center
 Hampton, Virginia, USA

Paul M.H.W. Vijgen
 High Technology Corporation
 Hampton, Virginia, USA

Jay D. Hardin
 North Carolina State University
 Raleigh, NC, USA

Abstract

As part of a multi-phased program for subsonic transport high-lift flight research, flight tests were conducted on the Transport Systems Research Vehicle (B737-100 aircraft) at the NASA Langley Research Center to obtain detailed flow characteristics of the high-lift flap system for correlation with computational and wind-tunnel investigations. Pressure distributions, skin-friction, and flow-visualization measurements were made on a triple-slotted flap system for a range of flap deflections, chord Reynolds numbers (10 to 21 million), and Mach numbers (0.16 to 0.36).

Experimental test results are given for representative flap settings indicating flow separation on the fore-flap element for the largest flap deflection. Comparisons of the in-flight flow measurements were made with predictions from available viscous multi-element computational methods modified with simple-sweep theory. Computational results overpredicted the experimentally measured pressures, particularly in the case involving separation of the fore flap, indicating the need for better modeling of confluent boundary layers and three-dimensional sweep effects.

Because of the importance of three-dimensional sweep effects on attachment-line and transitional flows near the leading-edge of multi-element high-lift systems, the potential for relaminarization of turbulent attachment-line flow and crossflow instability of the laminar boundary layer was studied using swept-wing boundary-layer methods.

Nomenclature

A	crossflow amplitude
A_o	crossflow amplitude at neutral point
b	wing span, ft
C_f	skin-friction coefficient, τ/q
C_L	lift coefficient, lift/qS
C_p	pressure coefficient, $(p-p_s)/q$
c	chord length, ft
\bar{c}	mean aerodynamic chord, 11.20 ft
f	frequency, Hz
h	pressure altitude, ft

K	relaminarization parameter, equation (1)
M	Mach number
n	logarithmic amplification ratio, $\ln(A/A_o)$
p	local static pressure, psf
p_s	freestream static pressure, psf
q	freestream dynamic pressure, $\rho V^2/2$, psf
$R_{\bar{c}}$	Reynolds number based on \bar{c} , $\bar{V}\bar{c}/\nu$
$R_{\theta,1}$	laminar attachment-line, momentum-thickness Reynolds number, $U_e \theta/\nu_e$
S	reference wing area, 980 ft ²
s	surface streamwise coordinate, ft
U_e	local edge velocity, ft/sec
V	true airspeed, ft/sec
V_i	indicated airspeed, knots
x/c	nondimensional chordwise coordinate
z/c	nondimensional thickness coordinate
α	aircraft angle of attack, deg
α_{2-D}	local streamwise angle of attack, deg
δ_f	flap deflection, deg
λ	crossflow instability wavelength, ft
ν	kinematic viscosity, ft ² /sec
ν_e	kinematic edge viscosity, ft ² /sec
ρ	air density, slugs/ft ³
θ	momentum thickness, ft
τ	shear stress, psf

Abbreviations

ESP	electronic scanning pressure
KIAS	knots indicated airspeed
TSRV	Transport Systems Research Vehicle
2-D	two-dimensional
3-D	three-dimensional

Introduction

Accurate prediction of surface-pressure distributions, merging boundary-layers, and separated-flow regions over multi-element high-lift airfoils is an essential requirement in the design of advanced high-lift systems for efficient subsonic transport aircraft.¹ The flow field around a multi-element wing with sweep is characterized by several aerodynamic properties which

are highly interrelated and complex in nature and presently not well understood (see Fig. 1).

Two-dimensional multi-element flow issues include the following:

- compressibility effects including shock/ boundary-layer interaction on the slat;
- laminar separation-induced transition along the upper surfaces;
- confluent boundary layer(s) - the merging and interacting of wakes from upstream elements with the boundary layers of downstream elements;
- cove separation and reattachment; and,
- massive flow separation on the wing/flap upper surfaces.

Three-dimensional multi-element flow issues include the following:

- leading-edge attachment-line transition;
- relaminarization of turbulent flow;
- crossflow instability transition downstream of the attachment line;
- sweep effects on confluent boundary-layer development, turbulent boundary-layer separation, and separated cove flows; and,
- highly three-dimensional, local flow modifications; e.g., vortex generators; flap side-edge-separated flows; and flow interactions with flap-track fairings, engine pylons, and landing-gear struts.

The availability of detailed measurements of pressure distributions and boundary-layer flow parameters at flight Reynolds and Mach numbers is critical to the evaluation of computational methods and to the modeling of turbulence structures for closure of the governing flow equations.^{2,3} The complexity of the multi-element flow field has generally limited detailed measurements and analyses to two-dimensional studies. Previous two-dimensional wind-tunnel investigations have included detailed flow measurements of the Reynolds-stress components at sub-scale Reynolds numbers and in two dimensions.^{4,5,6,7} These results have been applied towards the development and validation of 2-D multi-element numerical codes. However, availability of detailed data in three dimensions at full-scale Reynolds numbers has been very limited. To contribute to the understanding and correlation of high-lift research between wind tunnel, computational fluid dynamics (CFD), and flight, additional experimental data are needed at full-scale Reynolds number and for 3-D swept wings. Only a limited study has been conducted in flight for detailed flow measurements on a high-lift system.⁸ Further understanding of scale effects on 2-D and 3-D sub-scale wind-tunnel results is required to accurately extrapolate to 3-D, full-scale flight conditions.^{9,10,11,12}

As part of a multi-phased high-lift flight research program, flight tests were conducted using the NASA-

Langley Transport Systems Research Vehicle (TSRV), to obtain detailed full-scale flow measurements of the 5-element high-lift system at various flight conditions. Phase I of the flight program has been completed, and the investigation focussed on the flow characteristics of a triple-slotted flap system. Subsequent flight experiments in future phases of the research program will provide detailed measurements of full-chord pressure distributions as well as boundary-layer transition and turbulence measurements at several spanwise stations.

The purpose of this paper is threefold. First, an investigation of in-flight pressure, skin-friction, and flow-visualization measurements is presented for a high-lift flap system. Secondly, an analysis of the in-flight measurements using available two-dimensional, viscous multi-element airfoil codes is presented. Finally, the potential for attachment-line transition, relaminarization, and crossflow transition in the leading-edge region of the slat and main wing elements is presented using swept-wing boundary-layer stability theory.

Description of Flight Experiment

Test Aircraft

The NASA Langley TSRV is the prototype aircraft used in the development of the Boeing B737-100 and has been heavily modified for flight systems research.¹³ The Boeing 737-100 is a twin-jet, short-haul, subsonic transport designed to carry approximately 100 passengers with a cruise speed of Mach 0.78. In order to obtain short-field takeoff and landing performance, the aircraft incorporates a slat and triple-slotted flap high-lift system. Figure 2 shows the TSRV in flight while conducting the present high-lift experiments. Wind-tunnel investigations by NASA of the basic configuration aerodynamic characteristics for the Boeing 737-100 model have been documented.^{14,15}

A planform view of the B737-100 configuration is shown in figure 3. The aircraft wing is characterized by a span of 93 ft., an aspect ratio of 8.82, and a sweep angle of 25° at the quarter-chord line. The sweep angle of the wing leading-edge is 27.58°. Inboard leading-edge Krueger flaps and outboard leading-edge slats are extended in conjunction with the deflection of the triple-slotted trailing-edge flap system. As shown in figure 4, the high-lift wing section studied in this paper consists of 5 elements - the leading-edge slat, the main wing with fixed leading edge, the fore flap, the mid flap, and the aft flap. At flap settings of 30° and 40°, the two most outboard slat segments are fully extended and deflected an additional increment from the 15° and 25° setting (see fig. 4), effectively creating a spanwise break in the wing leading edge between the slats (see fig. 5). The coves in figure 4 are shown streamlined for computational purposes; in actuality, the cove shape is a trailing-edge cutout of the main-wing and mid-flap elements and is a cavity to house the subsequent flap element in the retracted position.

Instrumentation, Data Acquisition and Reduction

Flow-visualization, pressure-distributions, and skin-friction measurements were made on the outboard segment of the triple-slotted Fowler flap system of the research aircraft (see fig. 5). Flow visualization was conducted with nylon yarn tufts applied to the upper surfaces of the outboard flap elements and the aft surface of the main wing to indicate flow direction and local regions of flow separation. The tuft patterns were recorded with still and video photography to allow for post-flight analysis and correlation.

Streamwise static pressure distributions were obtained about each of the flap elements using thin belts of plastic tubing (0.062 inch outside diameter) wrapped around each of the three flap elements at two nominal spanwise stations (see fig. 5). The belts were attached to the surface with thin (0.005 inch) adhesive tape. With the installation of the pressure belts, the minimum possible flap deflection was limited to 15°, while the standard maximum flap deflection of 40° was unchanged. A control-surface potentiometer attached to the mid-flap provided deflection information under loading during the flight. A total of 160 pressure tubes were connected to five electronically scanning pressure (ESP) modules which were located in the wing cove region (see fig. 5). The ESP modules were maintained at a constant temperature to minimize zero shift of the measurement, and two differential-pressure transducer ranges (2.5 and 5 psi) allowed high resolution of the pressure data. A plenum chamber was housed in the wing cove region to provide the reference pressure for the ESP transducers; the reference pressure was monitored with an absolute pressure gauge and was related to the static pressure measured by the aircraft pitot-static probe. Six Preston tubes were installed near the trailing edge of each flap element as well as on the main wing element (see fig. 5). The modified Preston tube contains a static orifice in addition to the pitot pressure port. The measured pressure differential at the tube is converted to the local shear stress using the law-of-the-wall calibration assuming equilibrium turbulent flow.¹⁶

A small data-acquisition unit using single-board computer technology was developed to access and address the ESP transducers. The data-acquisition unit was located in the outboard flap track fairing of the wing (see fig. 5). The digital output data were transmitted to a small, portable on-board computer for real-time display and stored on an optical disk for post-flight playback and data analysis. Pressures were recorded at a rate of 10 samples per second while aircraft flight parameters were recorded at a rate of 20 samples per second. The pneumatic lag for a simulated pressure tube length was measured to be 0.5 seconds in ground tests.

An airspeed calibration flight with flaps deflected was conducted prior to the research flights using a tracking-radar method¹⁷ to provide corrections of the static pressure due to probe position error for each flap setting. These corrections along with temperature

measurements were used to compute freestream static and dynamic pressures, and Mach and Reynolds numbers. Lift coefficients were determined from steady-state, 1-g flight maneuvers using aircraft weight calculated from aircraft fuel consumption measured by flow meter sensors. In this Phase-I flight investigation, thrust corrections were not available for data reduction; however, the thrust contribution to the lift is considered small.

Flight Test Conditions

The flight tests covered a range of Reynolds and Mach numbers as the aircraft was flown to pressure altitudes of up to 20,000 feet. The chord Reynolds number, $R_{\bar{c}}$, ranged from 10 to 21 million, and the freestream Mach number varied from 0.16 to 0.36. Flap deflections of 15°, 25°, 30°, and 40° were investigated at pressure altitudes of 5,000 ft, 10,000 ft, 15,000 ft, and 20,000 ft. Figure 6 shows the test conditions and test points obtained in flight. Also, lines of constant Reynolds and Mach number are shown in figure 6 for standard atmospheric conditions. As indicated by figure 6, flight at increasing altitudes provide conditions of increasing Mach numbers and decreasing Reynolds number for a given indicated airspeed, V_i , approximately corresponding to a constant lift coefficient condition for constant aircraft weight.

The flight-test points were obtained for each of the flap settings at approximately 1-g, steady-state conditions (that is, vertical acceleration near zero) in level flight with the aircraft initially flown at a high nominal airspeed and then slowed to the stick-shaker speed. The research flight deck¹³ on the TSRV allowed auto-throttle and auto-pilot operations of the aircraft for airspeed- and altitude-hold modes of testing. Data were sampled for approximately 30 seconds at each constant-air-speed test point. In addition, data were recorded during the deceleration of the aircraft between selected test points. The aircraft was decelerated at a nominal rate of 1 knot per 5 seconds while constant altitude was maintained. Pertinent test points were repeated to ensure data repeatability. Data were obtained with the landing gear retracted.

Flight-Test Results and Discussion

Comparison with Wind-Tunnel Lift Data

A comparison of the present flight lift data for the four flap settings with available wind-tunnel lift data is shown in figure 7. The wind-tunnel investigation¹⁵ used a 1/8-scale model of the TSRV with flow-through nacelles, and the data were obtained for flap settings of 30° and 40° at $R_{\bar{c}} = 1.4$ million and $M = 0.14$. Trimmed lift coefficients were estimated from the wind-tunnel data. In the comparison of figure 7, the flight Reynolds numbers, $R_{\bar{c}}$, ranged from about 10 million at the low-speed, high-angle-of-attack conditions to about 21 million at high-speed, low-angle-of-attack conditions, depending on the flight altitude. In the mid-angle-of-attack range, lift values and incremental lift

values between flap deflections of 30° and 40° were similar between flight and wind tunnel (see fig. 7). In addition, the reduction in lift increment between the 30°- and 40°-flap settings above $\alpha \approx 8^\circ$ was observed in both flight and wind-tunnel data (see fig. 7). However, in the lower and higher angle-of-attack ranges, flight lift data differed from wind-tunnel lift data showing a higher lift-curve slope in flight. Moreover, the lift-curve slope in flight is nearly linear throughout the measured α range, whereas the lift curve slope from wind-tunnel data decreases with increasing angles of attack, indicating strong viscous effects.

At low angles of attack, the lift coefficients obtained in flight were overpredicted by the wind-tunnel data. This overprediction may be a result of a reversed Reynolds-number effect on multi-element airfoils as discussed in investigations by Woodward et al.¹⁸ and Morgan et al.¹⁹ where lift decreases at higher Reynolds number. Lift loss due to inverse Reynolds number effects is a result of the thinning of the boundary layer in the slot gaps at higher Reynolds numbers which causes the effective slot gaps to be no longer optimal for generating lift. At higher angles of attack ($\alpha \approx 10^\circ$ to 12°), the flight lift coefficients were severely underpredicted by the wind-tunnel data. This underprediction by the wind-tunnel data is likely due to premature viscous/separation effects at the lower Reynolds number experienced in the wind-tunnel.

Tuft Flow Visualization

Typical flow-visualization results are shown in figure 8 for two conditions with similar Reynolds and Mach numbers for the 15°- and 40°-flap settings. For the 15°-flap setting, the tuft photo is shown with the aircraft flown near the stick shaker speed ($V_i \approx 118$ KIAS, $\alpha \approx 12^\circ$). Even at this high-angle-of-attack condition, the flow on the flap surfaces appeared streamwise with no indication of separation along the span between the flap-track fairings (fig. 8a). For the 40°-flap setting, the tuft photo is shown with the aircraft flown near the stick shaker speed ($V_i \approx 105$ KIAS, $\alpha \approx 10^\circ$). For this high-lift condition, the flow patterns showed generally attached flow on the flap system, although, locally, in the wake of the flap track fairings, unsteady and separated flow regions are evident. In the region of the pressure belt locations, the flow remained attached on the main wing and the flaps except for flow separation near the trailing edge of the fore-flap element. The tuft patterns of figure 8b indicate that flow separation occurred over approximately the last 20 percent of the fore-flap chord. Figure 8b also indicates that the flow near the trailing edge of the aft flap is on the verge of separation at this condition. Finally, the flow near the flap/aileron edge shows the three-dimensional effect of unloading of lift as exhibited by the tuft patterns showing attached flow near the side-edge of the fore flap as well as the strong spanwise gradients in the trailing-edge region of each flap element due to the flap-edge vortical flow field.

Pressure Distributions

Representative pressure distributions measured in flight on the flap elements of the TSRV configuration are given in figures 9 and 10. In figure 9, the dominant effect of flap deflection on the pressure distributions is shown for flight conditions of $V_i \approx 130$ KIAS and $R_\tau \approx 14$ million. As expected, a significant increase in loading occurred with increasing flap deflection, with the highest loading occurring on the fore-flap element. The large change in mid-flap loading from 30°- to 40°-flap deflection corresponds to the large change in overlap between the fore-flap and the mid-flap elements (see fig. 4). The effect of angle of attack on the flap pressure distributions is shown in figure 10 for flap deflections of 15° and 40°. Note that both the Reynolds number and the Mach number varied as the angle of attack was changed. The data indicate little effect of angle of attack on the flap pressure distributions for the range of angles-of-attack attained. This result might be expected since the local angle of attack for each flap element depends largely on the in-flow angle as determined by the deflection angle of the flap system.

For the 40°-flap deflection, the pressure distribution correlates with tuft indications of separation near the trailing edge of the fore flap for $\alpha > 0^\circ$. In figure 10b, the separation is deduced from the near-constant pressure level near the trailing edge of the fore flap. Note that for the lowest angle of attack presented, the fore-flap pressures near the trailing edge do not indicate flow separation.

Skin-Friction Measurements

Figure 11 shows the in-flight skin-friction measurements obtained from the outboard Preston tubes near the trailing edge of the main and flap elements (fig. 5) as a function of angle of attack. The data of figure 11a indicate that at the flap setting of 40°, the skin-friction value is highest at the trailing edge of the main wing element. The flap elements exhibited lower skin-friction values than the main element apparently as a result of the steep adverse pressure recovery and possible confluent boundary-layer effects towards the trailing edge of the flaps.

On the fore-flap element for $\delta_f = 40^\circ$ and $\alpha \approx -0.5^\circ$, the skin-friction coefficient rapidly approached zero indicating that the flow was separated at the Preston-tube location. The separation behavior on the fore-flap element, as evidenced by the vanishing skin-friction coefficient, correlates with the results from tuft-flow visualization (fig. 8b) and the pressure distributions (fig. 10b). Since the changes in the Reynolds and Mach numbers are very small as α increased from -1.6° to 0° , the very rapid change in C_f near $\alpha \approx -0.5^\circ$ is deduced to be primarily an effect of angle of attack. As discussed, the initial adverse pressure gradient on the fore flap was nearly independent of the angle of attack (fig. 10b). The measured separation onset over the fore flap is likely caused by changes in the boundary-layer flow development over the slat and the main wing. As will be shown, large changes in pressure distribution are

predicted over the slat and the main element as α is varied.

Measured skin-friction values of the fore-flap element for various flap deflections are provided in figure 11b. Note that for given α , both $R_{\bar{c}}$ and M vary as the flap setting is changed. The data of figure 11b indicate that flow separation on the fore flap occurred only at the 40°-flap setting, however, the skin-friction variation with α is similar for the 30° and 40° geometries. Also the skin-friction variation with α for the 15° and 25° settings are similar, however, both show opposite trends compared to the higher settings. The changes in C_f behavior between the 25° and 30° setting could be caused by the additional slat deflection (see fig. 4), resulting in the presence of a significant slat wake along the main-element upper surface and a change in the flow over the fore flap. The presence of a strong slat wake can result in a confluent boundary layer over the fore flap with two distinct wake portions, and a reduction in wall shear stress over the flap is expected as a consequence.

Computational Analysis of Measurements

Analysis Approach

The current lack of three-dimensional confluent boundary-layer multi-element analysis methods, necessitates the use of two-dimensional methods in conjunction with simple-sweep theory.¹ In the present analysis, simple-sweep theory, described in the paper by Lock²⁰, is used to account for sweep effects. The sectional geometries used in the computational analyses are shown in figure 4. The actual cove shapes of the main element and the mid flap have been replaced by smoothly faired shapes to facilitate the flow calculations.

One of the challenges in the application of 2-D calculations to 3-D results is the determination of the local angle of attack, α_{2-D} , for the two-dimensional methods. As shown in the measurements in figure 10, the flap pressure distributions are relatively independent of aircraft angle of attack for given flap setting; therefore, for the present analysis, it was sufficient to estimate the local angle of attack from a vortex-lattice analysis. Local angles of attack were determined using the spanload lift distribution²¹ calculated by a vortex-lattice method for the TSRV wing with flaps deflected and accounting for the trimmed lift decrement of the horizontal tail (fig. 7). Preliminary evaluation of this procedure using recent measurements of the full-chord wing-section pressures on the TSRV aircraft validated this method for estimating the local wing angle of attack.²²

Multi-Component Analysis Methods

Two 2-D, viscous, multi-element codes were used in the analysis of the in-flight flow measurements over the TSRV flap system. The first method is the Multi-Component Airfoil (MCARF) computer code,^{23,24} a

widely-used aerodynamic analysis method for two-dimensional, multi-element airfoils. The method employs potential-flow and integral boundary-layer methods to predict the viscous-flow properties over multi-element airfoils. Potential-flow calculations with a compressibility correction are made by replacing the element surfaces with a distribution of constant-strength vortex and source panels. MCARF employs the Goradia integral, confluent boundary-layer model with modifications to allow prediction of the onset of separation of the confluent boundary layer.²⁵ The basic assumptions of the confluent boundary-layer model are that the static pressures normal to the element surface are constant, and that near the trailing edge of each element the confluent boundary layer has degenerated to an ordinary turbulent boundary layer. That is, a confluent boundary layer may contain only the wake of the closest upstream element. The potential and viscous flow solutions are coupled by adding the calculated boundary-layer displacement thickness to the geometry of each element after each potential-flow/viscous-flow iteration. This process is repeated a pre-determined number of times or until convergence of the solution has been reached. This weak inviscid/viscous coupling approach precludes analysis of flow regions with separation.

The second analysis method used was the MSES^{26,27} multi-element airfoil code, a recently developed extension of the compressible-flow ISES^{28,29} single-element airfoil code. A streamline-based Euler discretization and a two-equation integral boundary-layer formulation are coupled through the displacement thicknesses and solved simultaneously by a full Newton scheme. The streamline-based grid is modified as a part of the Newton iteration scheme. Displacement bodies based on the boundary-layer and wake-displacement thickness are used to displace the inviscid surface streamlines, and are incorporated into the grid after each iteration. In this manner, MSES can account for strong inviscid/viscous coupling such as occurs in transitional separation bubbles as well as in regions of moderate flow separation such as coves or near trailing edges. Version 1.2 of the MSES method used in this paper includes a model of the asymmetric wake shape occurring in multi-deck boundary-layer structures, however, a confluent boundary-layer model is not included in this version.

Comparison of Computations with Flight Data

Figure 12 shows the MCARF-predicted variation in the airfoil pressure distributions for a range of angles of attack for flap settings of 15° and 40°. As observed in the experiment, the predicted flap pressure distributions show little dependence on the angle of attack, while the slat and main airfoil do show large variations with α . Compared with the other elements, the fore flap exhibits the largest adverse pressure gradient at the 40°-flap setting.

The experimental and calculated flap pressure distributions are compared in figures 13a and b for the

15°- and 40°-flap settings, respectively. For the 15° case, with no separation measured or predicted, the agreement is fair. For the 40°-flap setting, the pressures over the fore flap are substantially overpredicted. On the lower flap surfaces, there is no confluence between upstream and downstream boundary layers, and good agreement is obtained. Upper surface pressures, however, tend to be overpredicted by MCARF as indicated by Omar et al.³⁰ in the application of the MCARF to the two-dimensional, low-Reynolds-number data for a 5-element geometry. This overprediction of the pressures for the 2-D case suggests that the confluent boundary-layer model may not be adequate for the present triple-slotted flap geometry.

Figure 14 presents MSES results obtained for the 40°-flap setting for comparison with flight measurements. The 200 x 50 computational grid for the 5-element system used by MSES to solve the Euler-flow equations, shown in figure 14a, clearly indicates stagnation streamlines, as well as a large closed-separation region on the lower slat surface. Figure 14b shows the predicted flow-separation regions as displacement regions for the Euler grid near the trailing edge of the fore flap and in the coves of the main wing and the mid flap. In addition, MSES predicts onset of separation just ahead of the trailing edge of the aft-flap element. Comparison of the streamwise predicted and measured pressure distribution over the flap system in figure 15 indicates that the direct inviscid/viscous MSES solution method properly models the measured separation near the trailing edge of the fore flap. The overprediction of the fore-flap upper-surface pressure distribution is slightly larger than by MCARF, and may be caused by the absence of a confluent model in the present MSES version.

Inclusion of a confluent boundary-layer model in MSES is needed to further address the significance of upstream wake interaction on the observed flap separation. Since the fore-flap separation onset is correctly predicted by both two-dimensional methods using simple-sweep theory, the separation phenomenon does not appear to be dominated by three-dimensional boundary-layer effects. The proper prediction of onset of trailing-edge separation over the fore flap by both MSES and MCARF at the 40°-flap setting also suggests that the separation is not dominated by confluent boundary-layer effects. The separation is apparently caused by the magnitude of the pressure recovery on the fore-flap surface at 40°. Note that the predicted magnitude of pressure gradient in the recovery is very similar to the gradient measured in flight (see figs. 13b and 15). The absence of 3-D effects in the analysis methods is likely to contribute to the present overprediction of the pressures over the forward portion of the flap.

Attachment-Line Transition, Relaminarization, and Crossflow Transition Prediction

In three-dimensional flows, transition can occur at higher Reynolds numbers at the attachment line near the leading edge, thereby, significantly influencing the downstream flow field, i.e. - confluent boundary layers and separated flows. Wind-tunnel and flight experiments to determine the state of the boundary layer over the swept leading edges of high-lift configurations reveal the presence of laminar, transitional, and turbulent flows along the attachment-line of the slat and fixed leading edge at certain test conditions.^{8,9,10} Depending on the pressure-distribution shape, leading-edge sweep angle and Reynolds number, the attachment line can be laminar, transitional, or turbulent.^{31,32} A possibility exists for relaminarization of the flow downstream of a turbulent attachment line if the streamwise flow acceleration is sufficiently strong.^{33,34} Boundary-layer crossflow is the primary cause of laminar instability and transition for swept wings without boundary-layer suction downstream of the leading edge,^{35,36,37,38} however, the presence and significance of crossflow instability and crossflow-induced transition in the leading edge regions of swept high-lift systems has not been studied with boundary-layer stability theory. If the flow ahead of the sharp adverse pressure gradient along the upper surface of the elements is laminar, significant Reynolds-number effects can occur due to the presence or absence of a laminar-separation bubble in this region. High-Reynolds-number wind-tunnel tests on swept wings indicated that maximum-lift losses of the order of 10 percent occurred when transition occurred in the leading-edge region.⁹ This issue is of significant importance in the extrapolation of sub-scale three-dimensional wind-tunnel results to flight Reynolds numbers, as well as in the analysis of future TSRV flight experiments.

Boundary-Layer Methods

In the absence of full 3-D multi-element, viscous-flow methods, the presented analysis of the measured flap pressures assumed essentially 2-D boundary-layer development with the simple-sweep correction. Current 3-D computational methods, however, do allow analysis of the laminar boundary layer flow along the leading edges of the high-lift elements not affected by confluent and merging boundary layers. The three-dimensional laminar boundary layer along the swept leading edges of the elements was computed using the compressible method by Kaups and Cebeci.³⁹ The boundary-layer equations are solved in a marching solution using the conical flow-field approximation for swept tapered wings. The program solves for the stagnation boundary-layer profile, provides the momentum Reynolds number, $R_{\theta,1}$, at the stagnation line, and is used in the present study to determine Launder's relaminarization parameter, K , in the streamwise direction. Finally, the method generates the derivatives

of the three-dimensional boundary-layer profiles for boundary-layer stability analysis.

The MARIA method⁴⁰ is used to estimate linear, stationary crossflow instability for incompressible flow conditions. The method utilizes crossflow instability charts, generated by an incompressible method⁴¹ that solves the full, three-dimensional, linear stability equations, to estimate local amplification rates for a range of crossflow instability wavelengths based on the local crossflow-shape factor and a crossflow Reynolds number. The amplification rates are integrated along the potential-flow streamline for each wavelength to obtain a spatial amplification factor. The interpolation-based stability method allows analysis of the global characteristics of the stationary crossflow instability; however, analysis of nonstationary instability waves, their orientation, as well as the small effects of compressibility requires solution of the stability equations. The COSAL method⁴² is used to solve the compressible linear parallel-flow stability equations for each 3-D mean-flow boundary-layer profile to determine the local growth rate, wave front direction, and wavelength for given instability frequency. The version of COSAL used in the present analysis does not include streamline- and surface-curvature terms in the stability equations.

Attachment-Line Transition and Relaminarization

Attachment-line transition and the possibility for relaminarization along the five elements of the B737-100 geometry are examined for the 40°-flap setting with $\alpha = 0^\circ$ and $M = 0.2$ for three chord-Reynolds numbers. Previous experimental studies at subsonic speeds along swept wings have shown that the attachment-line boundary layer can amplify instabilities and, thus, become turbulent if the laminar attachment-line, momentum-thickness Reynolds number, $R_{\theta,1}$, exceeds approximately 100. For $R_{\theta,1}$ below 100, turbulent disturbances propagating along the aft-swept attachment line (e.g., from the fuselage) are damped as they are convected along the leading edge, and the attachment line remains laminar. For $R_{\theta,1}$ exceeding 120, the attachment line is generally considered fully turbulent.^{31,32}

Using the predicted pressure distribution as given in figure 13b, $R_{\theta,1}$ was obtained for each element from the boundary-layer method. Table I indicates that the attachment line along the slat and fore flap are predicted to be laminar using the criterion of $R_{\theta,1} \approx 100$, while the attachment line along the fixed leading edge (main element) is likely to be turbulent at the conditions indicated. In a previous flight experiment, a laminar attachment line was measured along the slat of an Airbus A310 aircraft under certain high-lift flight conditions.⁸ For the 40°-flap setting, the stagnation point along the fixed leading edge is located well aft on the lower surface (fig. 12b) such that variation of α has only a small effect on $R_{\theta,1}$.

Table I. - $R_{\theta,1}$ at attachment line; $M = 0.2$, $\alpha = 0^\circ$, 40°-flap setting

$R_{\theta,1}$, million	10.0	15.0	20.0
Slat	67.4	82.6	95.4
Fixed	157.8	193.3	223.2
Fore	74.1	90.8	104.8
Mid	104.2	127.4	147.3
Aft	93.1	113.9	131.5

Lauder's relaminarization parameter³², K , has been used in previous studies on reversion from the turbulent state to the laminar state in two-dimensional flow, where

$$K = \frac{v_e}{U_e^2} \left(\frac{dU_e}{ds} \right) \cong \frac{1}{R_{\theta,1}} \left(\frac{V}{U_e} \right)^2 \frac{d(U_e/V)}{d(s/c)} \quad (1)$$

Based on Launder's criterion, reversion from turbulent to laminar flow is possible for K larger than 1×10^{-6} . For K larger than 3×10^{-6} , relaminarization is likely; and for K larger than 5×10^{-6} , complete relaminarization occurs.^{32,43} Figure 16 summarizes the predicted streamwise K values over the upper surface of the slat and main wing elements for the flap setting of 40° (condition corresponds to Table I). The abscissa is the distance along the potential-flow streamline starting at the stagnation point nondimensionalized by a constant reference chord. For the elements shown, as well as for the fore-, mid-, and aft-flap elements (not shown), values of $K > 3 \times 10^{-6}$ were predicted over a substantial region along the streamline, indicating that relaminarization is likely at the Reynolds numbers considered. Of particular significance is the prediction of relaminarization of the flow along the upper surface of the fixed leading-edge geometry at this condition. By contrast, the K parameter along the lower surface of the fixed leading edge of the main element is only of order 0.1×10^{-6} for this flap setting, and, consequently, if the attachment-line along the fixed leading edge is turbulent, relaminarization of the lower-surface-flow is unlikely.

Crossflow Instability

Provided the flow near the attachment line is laminar, transition of the laminar boundary layer along the upper surface of the swept high-lift elements ahead of the laminar-separation point can occur due to sufficiently large crossflow amplification. The crossflow instability amplification along the upper-surface streamline of the elements was analyzed for a range of crossflow wavelengths, λ/c . In boundary-layer stability theory, the crossflow amplification factor or

"n-factor", where $n = \ln(A/A_0)$, has been used to systematically correlate transition-onset locations observed in wind-tunnel and flight experiments. Application of the e^n transition-prediction method⁴⁴ to previous swept-wing wind-tunnel and flight experiments resulted in crossflow n-factors at transition in the range of 9 to 12, depending on the simultaneous presence of streamwise instability amplification.^{38,45} However, an n-factor below 9 can be expected in the presence of elevated ambient turbulence levels and surface roughness.

For the highest flap setting with $M = 0.2$, $\alpha = 0^\circ$ and $Re_c = 15$ million, figure 17 presents the predicted crossflow amplification along the upper-surface streamline of the slat and the main-element leading edge for the range of amplified wave-length ratios, λ/c , using the MARIA method. The calculations were continued up to the point of predicted laminar separation by the mean-flow method. If it is assumed that crossflow transition onset occurs when $n=9$ is reached, critical crossflow-instability amplification does not occur at this condition on the three elements. Based on these results, laminar flow and a transitional-separation bubble are expected in flight along the upper surface of the elements.

To verify the MARIA predictions in the present novel, high-lift application, the COSAL method was applied to the fixed leading-edge flow to analyze amplification factors for constant crossflow wavelengths. Figure 18 indicates that the MARIA method properly predicted the maximum n-factor ($n \approx 8.5$) in the flow, but indicated larger unstable wavelength ratios. COSAL analysis of the crossflow stability using the "envelope method" approach⁴⁶, whereby the local growth rate is maximized and the wave orientation and wavelengths are allowed to vary along the streamline, indicated that an n-factor of 8.6 is found for stationary ($f=0$) crossflow disturbances at the separation point. Recent tunnel experiments suggest that non-stationary waves can dominate the crossflow instability process in the presence of specific freestream turbulence. Generally, travelling frequencies have higher predicted amplification rates than the stationary crossflow waves^{36,47}, and an n-factor of 9.7 is found by COSAL for $f = 1000$ at $s/c = 0.15$ using the "envelope method" along the fixed leading edge. Depending on the n-factor that correlates with crossflow transition onset for the present condition, transition may occur just ahead of the pressure minimum over the fixed leading edge in flight. Investigation of these transition issues are planned in follow-on TSRV flight experiments.

Concluding Remarks

A flight experiment was conducted as the first part of a multi-phased subsonic transport high-lift research program for correlation with computational and ground-based wind-tunnel investigations. The flight program uses the NASA Langley TSRV (B737-100 aircraft) to

obtain global and detailed flow characteristics at full-scale Reynolds numbers to contribute to the understanding of several dominant high-lift flow issues such as boundary-layer transition, confluent boundary-layer development, and three-dimensional flow separation. The present flight experiment was conducted to obtain pressure distributions, skin-friction coefficients, and surface-flow visualization over the triple-slotted flap system of the research vehicle.

The flight-test results indicated that the lift curve was more linear, and the lift-curve-slope was larger for all flap settings in flight than that obtained in available sub-scale wind-tunnel tests. Tuft-flow visualization results indicated mostly undisturbed, unseparated flow over regions of the flaps away from the flap-track fairings and the flap/aileron junction for all but the highest flap setting. For the highest flap setting, flow separation was observed near the fore-flap trailing edge for angles of attack above approximately zero degrees, while no separation was observed at the lower flap settings. The measured surface-pressure distributions and skin-friction coefficients corroborated the flow-visualization results indicating separation on the fore-flap trailing edge. The measured flap pressure distributions showed little dependence on angle of attack, Reynolds number, or Mach number, but showed a large dependence on the flap setting.

MCARF and MSES, two-dimensional, viscous, multi-element airfoil methods, modified with simple sweep theory to correlate the two-dimensional predictions with the swept-wing flight measurements, were used to analyze the in-flight pressure and skin-friction measurements. Both methods overpredicted the suction-side pressure levels over the flaps, particularly over the fore flap. However, both methods predicted the location of onset of separation over the fore flap at the 40° -flap setting, and the MSES method properly predicted the constant pressure level in the separated-flow region. The pressure overprediction may be caused by the neglect of three-dimensional effects in the flow near the main element and the fore flap and the inadequacy of confluent boundary-layer modeling in the codes. The prediction of separation onset on the fore flap by both methods suggests that the separation is due to the steep adverse gradient, while confluent-flow effects are secondary. The inadequacies in the prediction of pressures for multi-element wing sections emphasizes the need to better understand confluent boundary-layers.

Because of the importance of leading-edge boundary-layer state on the development of downstream flow, the potential for relaminarization of turbulent flow and crossflow instability was investigated using swept-wing boundary-layer and boundary-layer stability methods. Analysis for a flap setting of 40° indicated that a laminar attachment line can be expected along the slat element. Using Launder's criterion, relaminarization of the upper-surface leading-edge flow was predicted along the upper surface of the fixed leading edge of the main element. Also, three-

dimensional boundary-layer analysis indicated that crossflow instability may not cause transition ahead of the onset of the laminar-separation point on the fixed leading edge. Based on these results, laminar-separation bubbles may occur in flight on the leading-edge upper surface of the main wing element. Additional analyses are required to further delineate the significance of crossflow instability, as well as the state of the attachment lines, for other flap settings and flight conditions. Since relaminarization and transition issues can be significant to maximum lift, flight experiments need to include detailed measurements of the transition locations in the leading-edge region of the high-lift elements.

Although the TSRV high-lift configuration employs a complex triple-slotted flap system, flight experiments on this configuration will provide detailed measurements that address several of the critical multi-element flow issues. With leading-edge and main-element geometries similar to those of modern designs, investigations of flow over the leading-edge, transition locations, the slat-cove flow, and the interaction of the slat wake with the boundary layer of the main and the fore-flap elements are of particular interest. Also, the triple-slotted trailing-edge flap system provides a challenging test case for CFD analysis, particularly in the modeling of 3-D confluent boundary layers and separation phenomena.

Further flight experiments are planned on the TSRV to obtain detailed full-chord wing pressures and boundary-layer measurements at full-scale Reynolds numbers for correlation and validation of wind-tunnel and computational research in high-lift systems aerodynamics.

Acknowledgements

The work of the second author was supported under NASA Langley Contract NAS 1-18240 and 1-19299. The authors acknowledge the assistance of Prof. Mark Drela of the Massachusetts Institute of Technology for providing the MSES code and for his assistance in the application of the code to a five-element configuration.

References

- ¹Dillner, B., May, F.W., and McMasters, J.H., "Aerodynamic Issues in the Design of High-Lift Systems for Transport Aircraft," AGARD-CP-365, May 1984.
- ²Brune, G. W., and McMasters, J. H., "Computational Aerodynamics Applied to High-Lift Systems," *Progress in Aeronautics and Astronautics: Applied Computational Aerodynamics*, Vol. 125, AIAA, New York, 1990, pp. 389 - 433.
- ³Bengelink, R.L., "The Integration of CFD and Experiment: An Industry Viewpoint (Invited Paper)," AIAA Paper 88-2043, May 1988.
- ⁴Olson, L.E., and Orloff, K. L., "On the Structure of Turbulent Wakes and Merging Shear Layers of Multi-Element Airfoils," AIAA Paper 81-1238, June 1981.

- ⁵Brune, G. W., and Sikavi, D. A., "Experimental Investigation of the Confluent Boundary Layer of a Multi-Element Low-Speed Airfoil," AIAA Paper 83-0566, January 1982.
- ⁶Braden, J.A., Whipkey, R.R., Jones, G.S., Lilley, D.E., "Experimental Study of the Separating Confluent Boundary-Layer," NASA CR-3655, June 1983.
- ⁷Nakayama, A., Kreplin, H.P., and Morgan, H.L., "Experimental Investigation of Flowfield About a Multi-element Airfoil," *AIAA Journal*, Vol. 28, No. 1, pp. 14-21, January 1990.
- ⁸Greff, E., "In-Flight Measurement of Static Pressures and Boundary Layer State with Integrated Sensors," *Journal of Aircraft*, Vol.28, May 1991, pp. 289-299.
- ⁹Kirkpatrick, D., and Woodward, D., "Priorities for High-Lift Testing in the 1990's," AIAA Paper 90-1413, June 1990.
- ¹⁰Garner, P.L., Meredith, P.T., and Stoner, R.C., "Areas for Future CFD Development as Illustrated by Transport Aircraft Applications," AIAA-91-1527-CP, June 1991.
- ¹¹Hardy, B. C., "Experimental Investigation of Attachment-Line Transition in Low-Speed High-Lift Wind-Tunnel Testing," AGARD CP 438, *Proceedings of the Symposium on Fluid Dynamics of Three-Dimensional Turbulent Shear Flows and Transition*, Turkey, October 1988, pp. 2-1 to 2-17.
- ¹²Valarezo, W.O., Dominik, C.J., McGhee, R.H., Goodman, W.L., Paschal, K.B., "Multi-Element Airfoil Optimization for Maximum High-Lift Reynolds Number," AIAA Paper 91-3332, September 1991.
- ¹³White, J.J., "Advanced Transport Operating Systems Program," SAE Paper 901969, October 1990.
- ¹⁴Capone, Francis J., "Longitudinal Aerodynamic Characteristics of a Twin-Turbofan Subsonic Transport with Nacelles Mounted Under the Wings," NASA TN D-5971, October 1970.
- ¹⁵Paulson, J.W., "Wind-Tunnel Results of the Aerodynamic Characteristics of a 1/8-Scale Model of a Twin-Engine Short-Haul Transport," NASA TM X-74011, April 1977.
- ¹⁶Bertelrud, A. "Total Head/Static Measurement of Skin Friction and Surface Pressure," *AIAA Journal*, Vol. 15, No. 3, March 1977, pp. 436-438.
- ¹⁷Gracey, W., "Measurement of Aircraft Speed and Altitude," NASA RP 1046, May 1980.
- ¹⁸Morgan, H.L., Ferris, J.C., and McGhee, R.J., "A Study of High-Lift Airfoils at High Reynolds Numbers in the Langley Low-Turbulence Pressure Tunnel," NASA TM 89125, July 1987.
- ¹⁹Woodward, D.S., Hardy, B.C., and Ashill, P.R., "Some Types of Scale Effect in Low-Speed High-Lift Flows," ICAS Paper 4.9.3, 1988.
- ²⁰Lock, R.C., "Equivalence Law Relating Three- and Two-Dimensional Pressure Distribution," ARC R&M 3346, May 1962.
- ²¹Vicroy, D.D., "The Aerodynamic Effect of Heavy Rain on Airplane Performance," AIAA Paper 90-3131-CP, September 1990.
- ²²Hardin, J.D., "Computational Aerodynamic Analysis of a Transport High-Lift System and Comparison with Flight Measurements," Master's thesis, North Carolina State University, May 1992.

- ²³Stevens, W.A., Goradia, S. H., and Braden, J. A., "Mathematical Model for Two-Dimensional Multi-Component Airfoils in Viscous Flows," NASA CR-1843, 1971.
- ²⁴Brune, G.W., Manke, J.W., "An Improved Version of the NASA-Lockheed Multielement Airfoil Analysis Computer Program," NASA CR-145323, 1978.
- ²⁵Morgan, H. L., Jr., "A Computer Program for the Analysis of Multielement Airfoils in Two-Dimensional Subsonic, Viscous Flow," NASA SP-347, March 1975, pp. 713 - 747.
- ²⁶Drela, M., "Newton Solution of Coupled Viscous/Inviscid Multi-Element Airfoil Flows," AIAA Paper 90-1470, June 1990.
- ²⁷Drela, M., "A User's Guide to MSES V1.2," MIT Computational Fluid Dynamics Laboratory, July 1991.
- ²⁸Giles, M.B. and Drela, M., "Two-Dimensional Transonic Aerodynamic Design Method," *AIAA Journal*, Vol. 25, No. 9, September 1987, pp.1199-1206.
- ²⁹Drela, M. and Giles, M.B. "Viscous-Inviscid Analysis of Transonic and Low Reynolds Number Airfoils," *AIAA Journal*, Vol. 25, No. 10, October 1987, pp. 1347-1355.
- ³⁰Omar, E., Zierten, T., Hahn, M., Szpiro, E., and Mahal, A., "Two-Dimensional Wind-Tunnel Tests of a NASA Supercritical Airfoil with Various High-Lift Systems, Volume II - Test Data," NASA CR-2215, September 1973.
- ³¹Pfenninger, W., "Laminar Flow Control Laminarization, USAF and NAVY Sponsored Northrop LFC Research Between 1949 and 1967," in *Special Course on Concepts for Drag Reduction*, AGARD Report No. 654, March 1977, pp. 3-1 to 3-75.
- ³²Poll, D. I. A., "Transition in the Infinite-Swept Attachment-Line Boundary-Layer," *The Aeronautical Quarterly*, Vol. 30, part 4, November 1979, pp. 607 - 629.
- ³³Lauder, B. E., and Jones, W. P., "On the Prediction of Relaminarization," ARC CP 1036, 1969.
- ³⁴Arnal, D., and Juillen, J. C., "Leading-Edge Contamination and Relaminarization on a Swept Wing at Incidence," *Fourth Symposium on Numerical and Physical aspects of Aerodynamic Flows*, edited by T. Cebeci, Cal. State University, Long Beach, CA, January 1989. 11 p.
- ³⁵Owen, P. R., and Randall, D. J., "Boundary-Layer Transition on a Swept Back Wing," RAE TM Aero 257, 1952.
- ³⁶Saric, W. S., and Reed, H. L., "Stability and Transition of Three-Dimensional Boundary Layers," AGARD CP 438, *Proceedings of the Symposium on Fluid Dynamics of Three-Dimensional Turbulent Shear Flows and Transition*, Turkey, October 1988, pp 1-1 to 1-20.
- ³⁷Runyan, L. J., Navrasan, B. H., and Rozendaal, R. A., "F-111 Natural Laminar Flow Glove Flight Test Data Analysis and Boundary-Layer Stability Analysis," NASA CR-166051, October 1983.
- ³⁸Obara, C. J., Vijgen, P.M.H.W., and Lee, C. C., "Analysis of Flight-Measured Boundary-Layer Stability and Transition Data," AIAA Paper 91-3282, September 1991.
- ³⁹Kaups, K., and Cebeci, T., "Compressible Laminar Boundary Layers with Suction on Swept and Tapered Wings," *Journal of Aircraft*, Vol. 14, No. 7, July 1977, pp. 661 - 667.
- ⁴⁰Dagenhart, J. R., "Amplified Crossflow Disturbances in the Laminar Boundary Layer on Swept Wings with Suction," NASA TP 1902, 1981.
- ⁴¹Srokowski, A.J., and Orszag, S. A., "Mass Flow Requirements for LFC Wing Design," AIAA Paper 77 - 1222, August 1977.
- ⁴²Malik, M. R., "COSAL - A Black-Box Compressible Stability Analysis Code for Transition Prediction in Three-Dimensional Boundary Layers," NASA CR 165925, May 1982.
- ⁴³Beasley, J. A., "Calculation of the Laminar Boundary Layer and Prediction of Transition on a Sheared Wing," RAE Technical Report 73156, 1974.
- ⁴⁴Hefner, J. N., and Bushnell, D. M., "Status of Linear Boundary-Layer Stability Theory and the e^n Method, With Emphasis on Swept-Wing Applications," NASA TP 1645, 1980.
- ⁴⁵Bushnell, D. M., Malik, M. R., and Harvey, W. D., "Transition Prediction in External Flows via Linear Stability Theory," IUTAM Symposium Transsonicum III, Goettingen, May 1988.
- ⁴⁶Malik, M. R., "Stability Theory for Laminar Flow Control Design," in *Viscous Drag Reduction in Boundary Layers*, Ed. D. Bushnell and J. Hefner, Progress in Astronautics and Aeronautics, Vol. 123, AIAA Washington D.C., 1990, pp. 3 - 46.
- ⁴⁷Nitsche-Kowsky, P., and Bippes, H., "Instability and Transition of a Three-Dimensional Boundary Layer on a Swept Flat Plate," *Phys. Fluids*, Vol. 31, No. 4, April 1988, pp. 786 - 795.

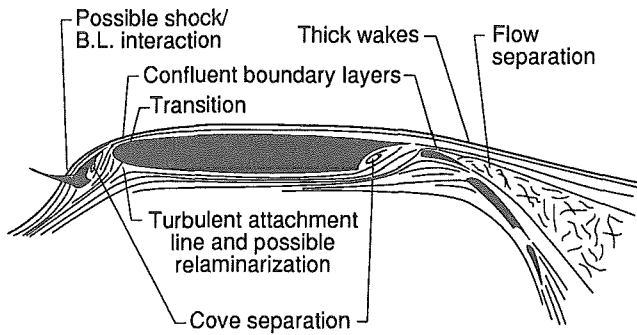


Figure 1.- Multi-element airfoil flow issues.

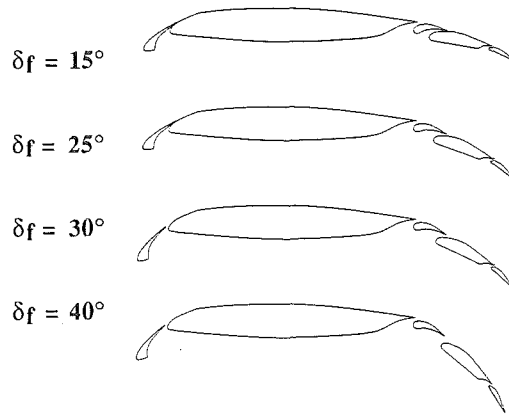


Figure 4. - Multi-element wing section geometry of the TSRV (737-100 aircraft) for four flap settings.



Figure 2. - NASA Langley TSRV (737-100 aircraft) in flight test of high-lift flap system aerodynamics.

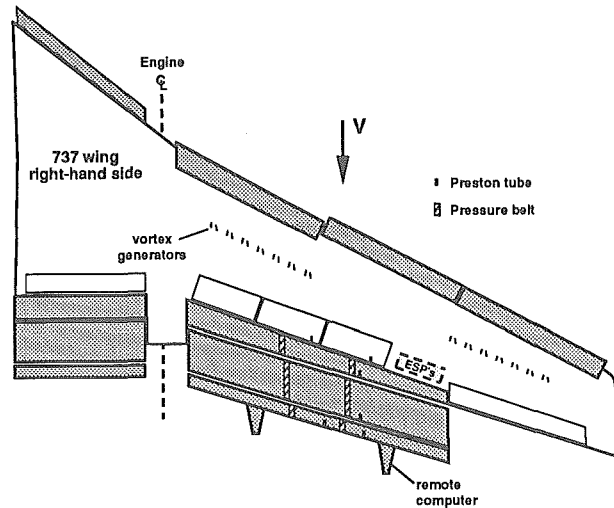


Figure 5. - High-lift instrumentation layout on the TSRV (737-100 aircraft). Wing planform illustrated at 40° flap position.

$S = 980.0 \text{ sq. ft.}$

$b = 93.0 \text{ ft.}$

$\bar{c} = 11.20 \text{ ft.}$

$\lambda_{i.e.} = 27.58^\circ$

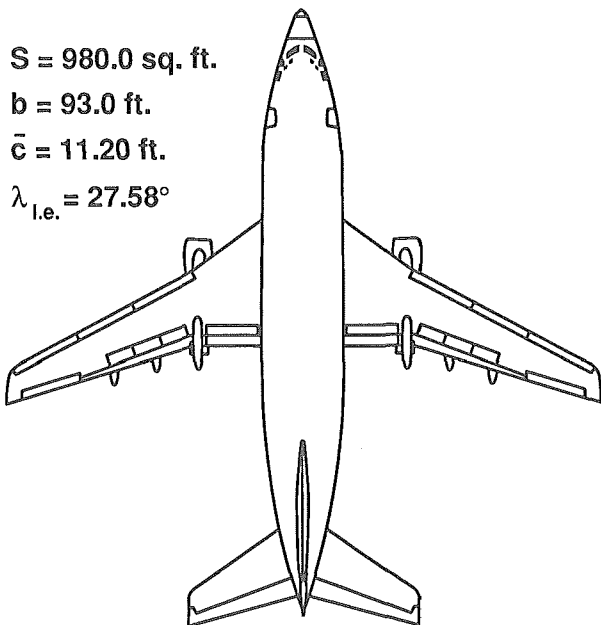


Figure 3. - Planform view of the TSRV (737-100 aircraft).

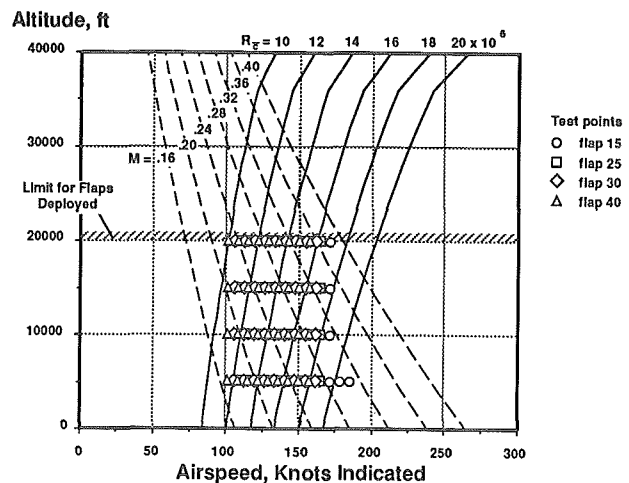


Figure 6. - High-lift, flight-test conditions and test points.

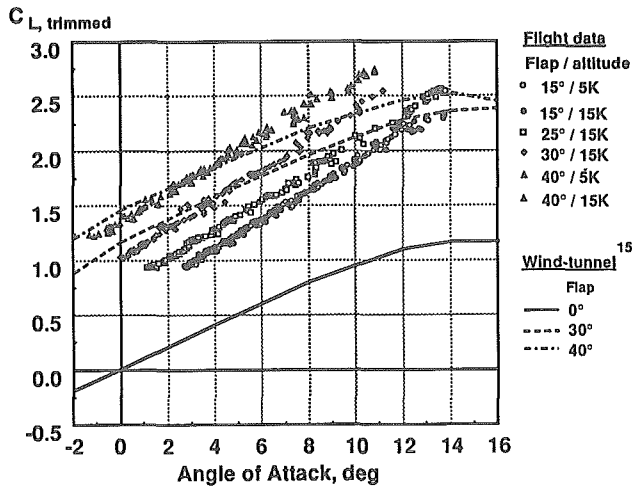
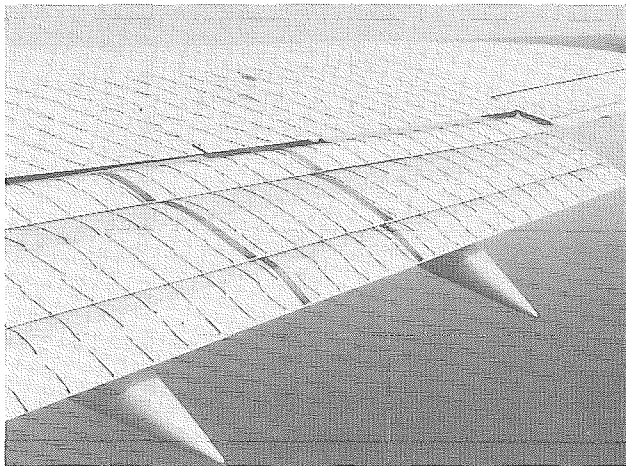
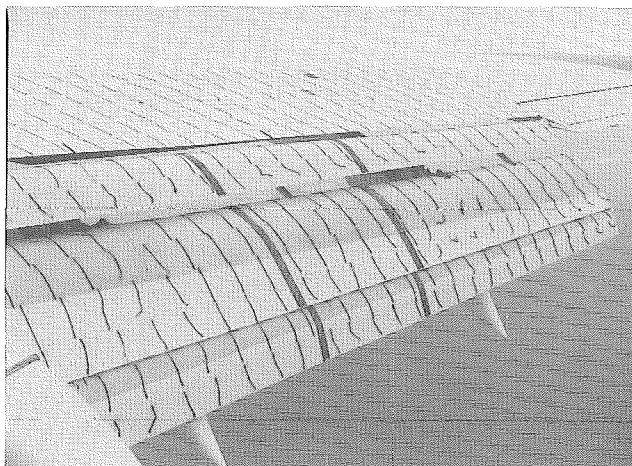


Figure 7. - Flight and wind-tunnel lift data comparison.



a) $\delta_f = 15^\circ$, $\alpha \approx 12^\circ$, $R_{\bar{c}} \approx 12$ million, $M \approx 0.20$

Figure 8. - In-flight tuft flow visualization.



b) $\delta_f = 40^\circ$, $\alpha \approx 10^\circ$, $R_{\bar{c}} \approx 13$ million, $M \approx 0.21$

Figure 8. - Concluded

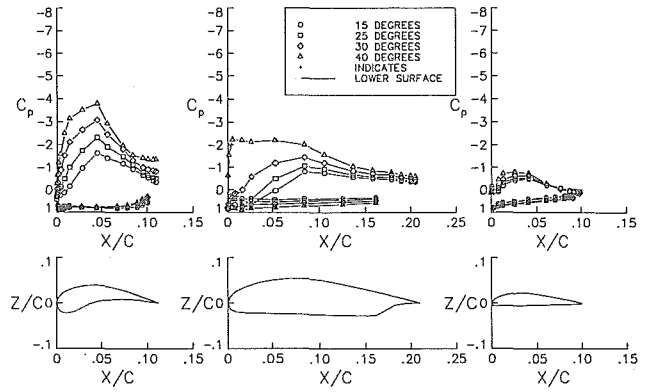
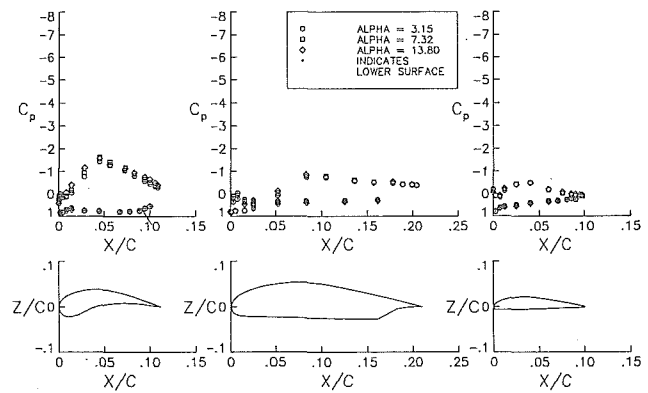
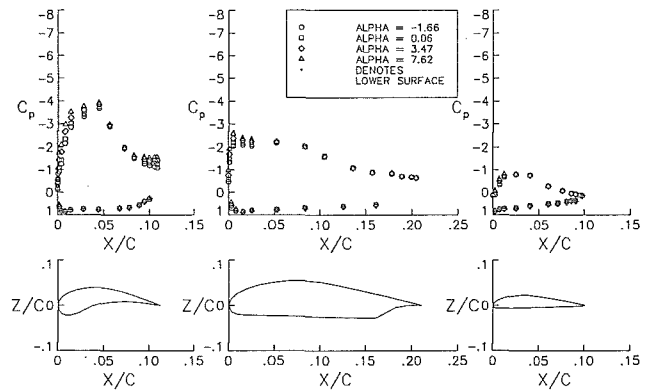


Figure 9. - Effect of flap deflection on flap pressure distributions. $V_i \approx 130$ KIAS, $h = 5,000$ ft., $R_{\bar{c}} \approx 14.5$ million, $M \approx 0.22$.



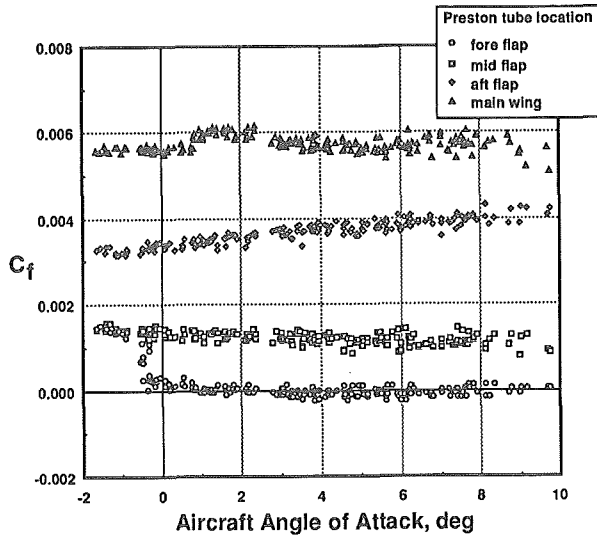
a) $\delta_f = 15^\circ$, $R_{\bar{c}} = 12 - 22$ million, $M = 0.18 - 0.30$

Figure 10. - Effect of angle of attack on flap pressure distributions. $h = 5,000$ ft.

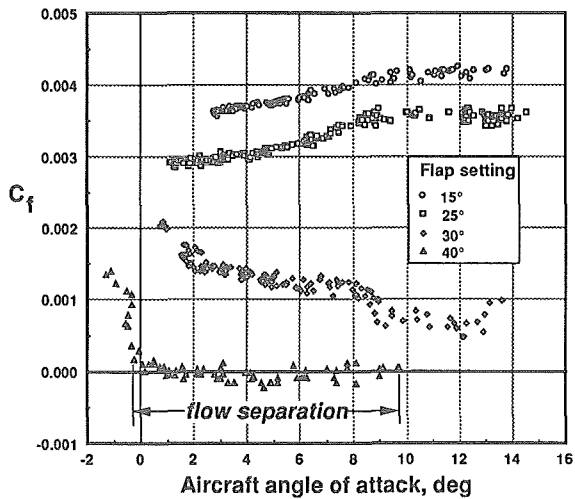


b) $\delta_f = 40^\circ$, $R_{\bar{c}} = 11 - 18$ million, $M = 0.17 - 0.25$

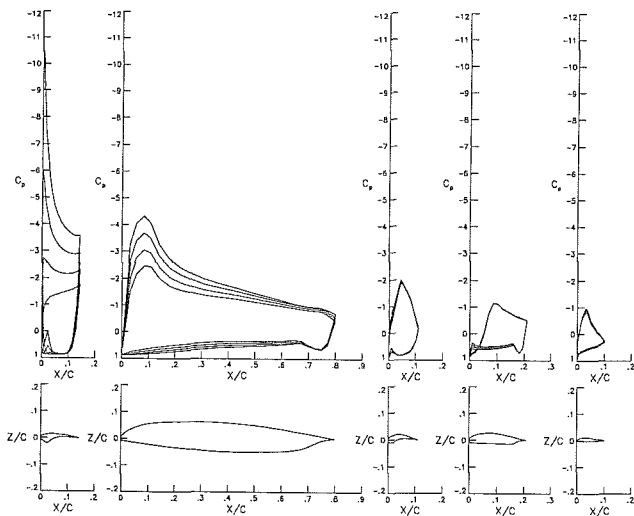
Figure 10. - Concluded



a) Main- and flap-element trailing edges, $\delta_f = 40^\circ$
 Figure 11. - Skin-friction measurements, $h = 5,000$.

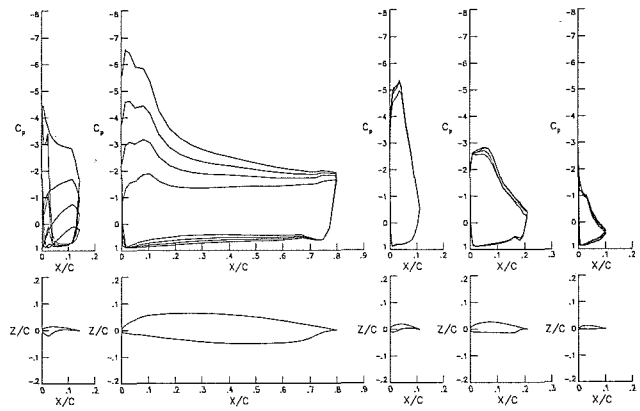


b) Fore-flap trailing edge, $\delta_f = 15^\circ, 25^\circ, 30^\circ,$ and 40°
 Figure 11. - Concluded.



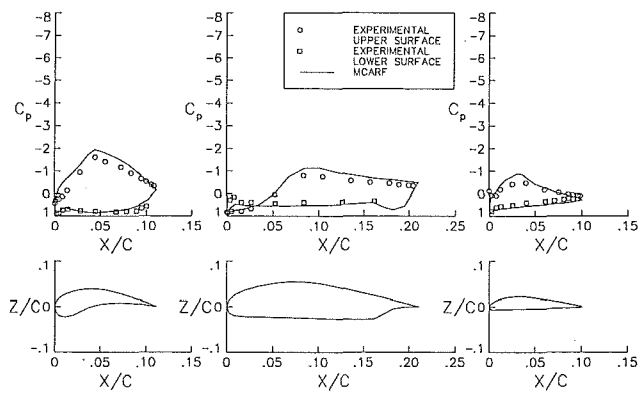
a) $\delta_f = 15^\circ$; $\alpha_{2-D} = 3^\circ, 6^\circ, 9^\circ, 12^\circ$; $R_{\bar{c}} \approx 14.5$ million, $M = 0.21$

Figure 12. - Predicted effect of angle of attack on pressure distributions (MCARF).



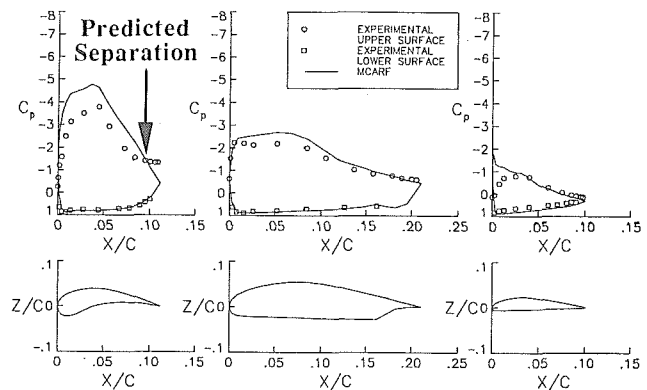
b) $\delta_f = 40^\circ$; $\alpha_{2-D} = -10^\circ, -5^\circ, 0^\circ, 5^\circ$; $R_{\bar{c}} \approx 14.5$ million, $M = 0.21$

Figure 12. - Concluded.



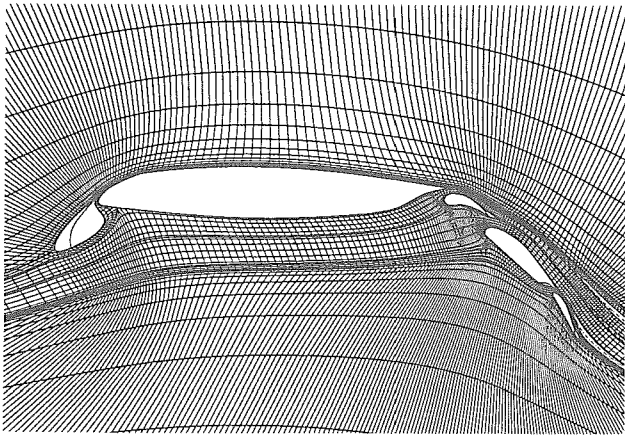
a) $\delta_f = 15^\circ$, $\alpha \approx 10^\circ$, $R_{\bar{c}} \approx 14.5$ million, $M = 0.21$.

Figure 13. - Comparison of MCARF pressure distributions with flight measurements.



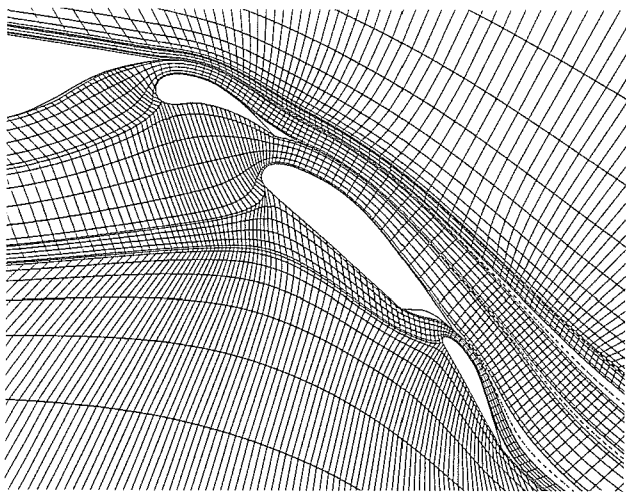
b) $\delta_f = 40^\circ$; $\alpha \approx 3^\circ$; $R_{\bar{c}} \approx 14.5$ million, $M=0.21$.

Figure 13. - Concluded.



a) Computational grid

Figure 14. - MSES computations of a 5-element high-lift system, $\delta_f = 40^\circ$, $\alpha = 6.03^\circ$, $R_{\bar{c}} = 10.9$ million, $M = 0.25$.



b) separated flow regions

Figure 14. - Concluded.

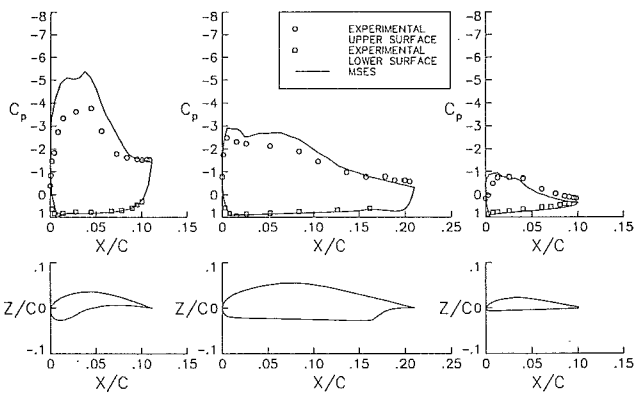
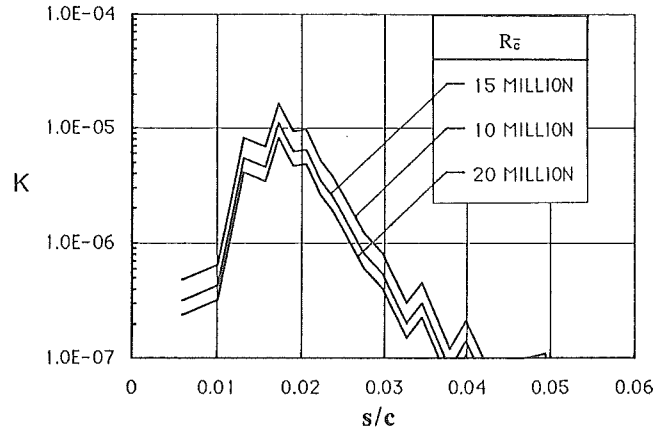
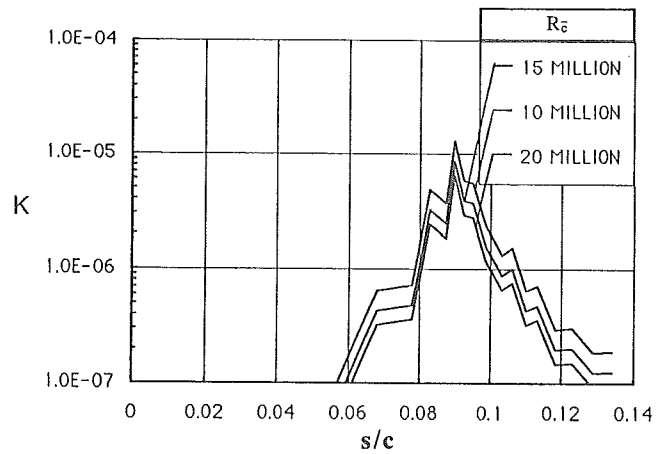


Figure 15. - Comparison of MSES computations with flight pressure distributions, $\delta_f = 40^\circ$, $\alpha = 6.03^\circ$, $R_{\bar{c}} = 10.9$ million, $M = 0.25$.



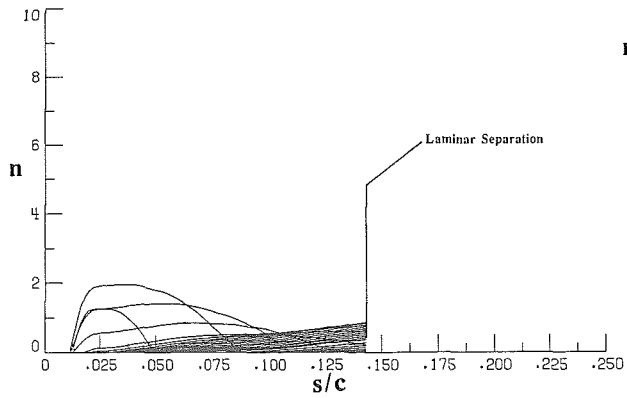
a) slat upper - surface streamline

Figure 16. - Leading-edge relaminarization parameter for $\delta_f = 40^\circ$, $\alpha_{2-D} = 0^\circ$, $M = 0.2$.



b) main element upper - surface streamline

Figure 16. - Concluded.



a) slat upper - surface streamwise amplification

Figure 17. - Cross-flow stability predictions for $\delta_f = 40^\circ$, $\alpha_{2-D} = 0^\circ$, $R\bar{c} = 15$ million, $M = 0.2$.

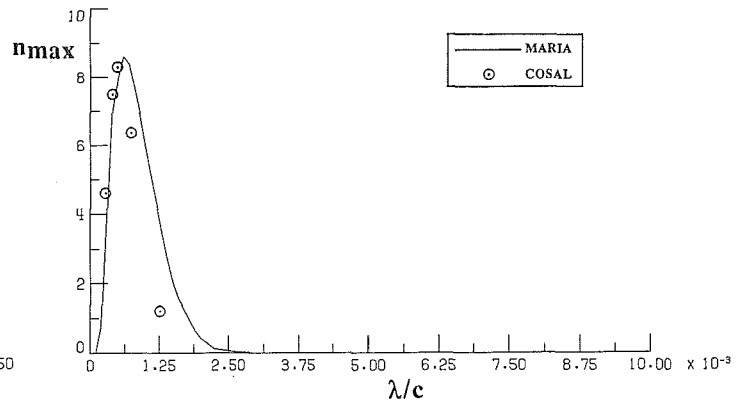
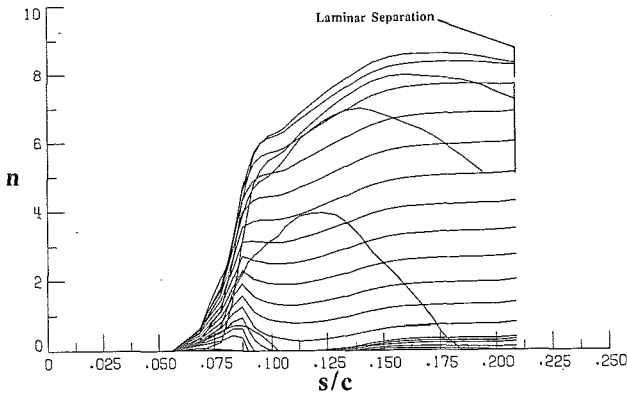


Figure 18. - Comparison of MARIA and COSAL predictions of n_{MAX} .



b) main element upper - surface streamwise amplification

Figure 17. - Concluded.